



## Article

# Biaxial Tensile Strain-Induced Enhancement of Thermoelectric Efficiency of $\alpha$ -Phase $\text{Se}_2\text{Te}$ and $\text{SeTe}_2$ Monolayers

Shao-Bo Chen <sup>1,2</sup>, Gang Liu <sup>3</sup>, Wan-Jun Yan <sup>2</sup>, Cui-E Hu <sup>4,\*</sup>, Xiang-Rong Chen <sup>1,\*</sup> and Hua-Yun Geng <sup>5</sup>

<sup>1</sup> College of Physics, Institute of Atomic and Molecular Physics, Sichuan University, Chengdu 610064, China; shaobochoen@yeah.net

<sup>2</sup> College of Electronic and Information Engineering, Anshun University, Anshun 561000, China; yanwanjun7817@163.com

<sup>3</sup> School of Physics and Engineering, Henan University of Science and Technology, Luoyang 471023, China; liugang8105@haust.edu.cn

<sup>4</sup> College of Physics and Electronic Engineering, Chongqing Normal University, Chongqing 400047, China

<sup>5</sup> National Key Laboratory for Shock Wave and Detonation Physics Research, Institute of Fluid Physics, CAEP, Mianyang 621900, China; s102genghy@caep.cn

\* Correspondence: cuiehu@cqnu.edu.cn (C.-E.H.); xrchen@scu.edu.cn (X.-R.C.)

**Abstract:** Thermoelectric (TE) materials can convert waste heat into electrical energy, which has attracted great interest in recent years. In this paper, the effect of biaxial-tensile strain on the electronic properties, lattice thermal conductivity, and thermoelectric performance of  $\alpha$ -phase  $\text{Se}_2\text{Te}$  and  $\text{SeTe}_2$  monolayers are calculated based on density-functional theory and the semiclassical Boltzmann theory. The calculated results show that the tensile strain reduces the bandgap because the bond length between atoms enlarges. Moreover, the tensile strain strengthens the scattering rate while it weakens the group velocity and softens the phonon model, leading to lower lattice thermal conductivity  $k_l$ . Simultaneously, combined with the weakened  $k_l$ , the tensile strain can also effectively modulate the electronic transport coefficients, such as the electronic conductivity, Seebeck coefficient, and electronic thermal conductivity, to greatly enhance the  $ZT$  value. In particular, the maximum n-type doping  $ZT$  under 1% and 3% strain increases up to six and five times higher than the corresponding  $ZT$  without strain for the  $\text{Se}_2\text{Te}$  and  $\text{SeTe}_2$  monolayers, respectively. Our calculations indicated that the tensile strain can effectively enhance the thermoelectric efficiency of  $\text{Se}_2\text{Te}$  and  $\text{SeTe}_2$  monolayers and they have great potential as TE materials.

**Keywords:** biaxial-tensile strain;  $\alpha$ -phase structure; lattice thermal conductivity; thermoelectricity



**Citation:** Chen, S.-B.; Liu, G.; Yan, W.-J.; Hu, C.-E.; Chen, X.-R.; Geng, H.-Y. Biaxial Tensile Strain-Induced Enhancement of Thermoelectric Efficiency of  $\alpha$ -Phase  $\text{Se}_2\text{Te}$  and  $\text{SeTe}_2$  Monolayers. *Nanomaterials* **2022**, *12*, 40. <https://doi.org/10.3390/nano12010040>

Academic Editor: Gyaneshwar P. Srivastava

Received: 4 November 2021

Accepted: 17 December 2021

Published: 23 December 2021

**Publisher's Note:** MDPI stays neutral with regard to jurisdictional claims in published maps and institutional affiliations.



**Copyright:** © 2021 by the authors. Licensee MDPI, Basel, Switzerland. This article is an open access article distributed under the terms and conditions of the Creative Commons Attribution (CC BY) license (<https://creativecommons.org/licenses/by/4.0/>).

## 1. Introduction

Thermoelectric materials have drawn considerable attention because they can harvest energy from waste heat by converting thermal energy directly into electrical energy [1–3]. The conversion efficiency of a TE material can be evaluated by the dimensionless figure of merit,  $ZT = S^2\sigma T / (k_e + k_l)$ , where  $S$ ,  $\sigma$ ,  $T$  are the Seebeck coefficient, the electrical conductivity, and the absolute temperature, respectively.  $k_e$  and  $k_l$  are electronic and lattice thermal conductivities. High thermoelectric performance requires a large thermoelectric power factor ( $\text{PF} = S^2\sigma$ ) and low thermal conductivity. However, the intrinsic relationship among these crucial parameters makes it difficult to improve the  $ZT$  value of a TE material.

In 2017, Zhu et al. [4] and Chen et al. [5] predicted and successfully synthesized the tellurene on highly oriented pyrolytic graphite (HOPG) substrates by using molecular beam epitaxy. Subsequently, a new two-dimensional (2D) materials family, the group-VI elemental 2D materials, has attracted significant attention due to its high carrier mobility, high photoconductivity, and thermoelectric responses [6–11]. Recent studies confirmed that the compounds composed of Te and Se have excellent thermoelectric and electronic transport properties [7,8,12]. In our previous work [7], we revealed that the 1T-phase  $\text{Se}_2\text{Te}$  and  $\text{SeTe}_2$  monolayers are promising medium-temperature thermoelectric materials;

however, their room temperature conversion efficiency is inferior. Recently, numerous studies [13–16] proved that the tensile mechanic strain can induce the reduction of the lattice thermal conductivity and then enhancement of the thermoelectric performance of 2D materials. Therefore, expecting to enhance the low-temperature thermoelectric efficiency, we here investigate the effect of biaxial tensile strain on the properties of  $\alpha$ -phase Se<sub>2</sub>Te and SeTe<sub>2</sub> monolayers.

In this paper, the small biaxial-tensile strain effects on electronic properties, lattice thermal conductivity, and thermoelectric performance of  $\alpha$ -phase Se<sub>2</sub>Te and SeTe<sub>2</sub> monolayers are calculated by first-principles calculations combined with the semiclassical Boltzmann theory. The calculated results indicate that the tensile strain results in lower lattice thermal conductivity by strengthening the scattering rate while at the same time weakening the group velocity and softening the phonon model. Additionally, the  $ZT$  value is visibly enlarged upon applied tensile strain; for example, the maximum n-type doping  $ZT$  under 1% and 3% strain increases up to six and five times higher than the corresponding  $ZT$  without strain for the Se<sub>2</sub>Te and SeTe<sub>2</sub> monolayers, respectively. Our calculations confirm that the tensile strain is an effective way to enhance the thermoelectric efficiency of Se<sub>2</sub>Te and SeTe<sub>2</sub> monolayers, which can stimulate further experimental works.

## 2. Theoretical Methods and Computational Details

All calculations are based on the first-principles calculations implemented in the Vienna ab initio Simulation Package (VASP) code [17,18] in the framework of the density functional theory (DFT). To solve the Kohn–Sham equations, the generalized gradient approximation (GGA) within the Perdew–Burke–Ernzerhof (PBE) formulation [19] or the B3LYP(B3PW) [20,21] is widely used to describe exchange-correlation potential. In this study, we used the former method to describe the exchange-correlation potential. A plane wave cutoff was set to 500 eV, and dense k-meshes of  $14 \times 14 \times 1$  and  $22 \times 22 \times 1$  were used to sample the Brillouin zone for structure optimizations and electronic property calculations, respectively. A vacuum space larger than 15 Å was used to avoid interactions of the nearest layers. The structures were fully optimized until the convergence threshold for electronic and ionic relaxations reached  $10^{-8}$  eV and  $10^{-3}$  eV/Å, respectively. The spin-orbit coupling (SOC) was taken into account in all calculations of the electronic properties.

Recently, Yang’s group developed a new TransOpt code [22] for calculating the electron transport properties based on semi-empirical Boltzmann equation with a constant electron–phonon coupling approximation. The advantage of TransOpt is not only more accurate than the constant relaxation time approximation (CRTA) but also can effectively avoid band crossing problems. Numerous studies [22–26] demonstrated that TransOpt is reasonable for calculating the transport properties and can be used in high-throughput calculations. In general, the Seebeck coefficient  $S$  and electrical conductivity  $\sigma$  are evaluated by the formula as followed [27–30]

$$S(\mu, T) = \frac{ek_B}{\sigma} \int d\varepsilon \left( -\frac{\partial f_\mu(T, \varepsilon)}{\partial \varepsilon} \right) \Xi(\varepsilon) \frac{\varepsilon - \mu}{k_B T} \quad (1)$$

$$\sigma(\mu, T) = e^2 \int d\varepsilon \left( -\frac{\partial f_\mu(T, \varepsilon)}{\partial \varepsilon} \right) \Xi(\varepsilon) \quad (2)$$

where  $f_\mu(T, \varepsilon)$ ,  $k_B$ ,  $e$ , and  $\varepsilon$  are the Fermi–Dirac distribution function, Boltzmann constant, electric charge, and band energy, respectively. The transport distribution is derived as  $\Xi(\varepsilon) = \sum_k v_k \otimes v_k \tau_k$ , where  $v_k$  and  $\tau_k$  are the group velocity and relaxation time at state  $k$ , respectively.  $\tau_k$  is a vital parameter to accurately calculate  $\sigma$  under the CRTA, which depends on the scattering mechanisms including phonon, impurity, and defect scatterings.

If only the intrinsic electron–phonon scatterings are considered, the relaxation time can be defined as [22,31,32]

$$\frac{1}{\tau_{nk}} = \frac{2\pi}{\hbar} \sum_{mk'\lambda} |g_{mk',nk}^\lambda|^2 \{ [f_{mk'} + n_{\mathbf{q}\lambda}] \delta(\varepsilon_{mk'} - \varepsilon_{nk} - \hbar\omega_{\mathbf{q}\lambda}) \delta_{\mathbf{k}+\mathbf{q},k'} + [1 + n_{\mathbf{q}\lambda} - f_{mk}] \delta(\varepsilon_{mk'} - \varepsilon_{nk} + \hbar\omega_{\mathbf{q}\lambda}) \delta'_{\mathbf{k}-\mathbf{q},k'} \}, \quad (3)$$

where  $|g_{mk',nk}^\lambda|$  describes the electron–phonon coupling matrix;  $f_{mk'}$  ( $f_{mk}$ ) is the Fermi–Dirac distribution for band-index  $m$  and wave-vector  $\mathbf{K}$ ;  $\delta(\varepsilon_{mk'} - \varepsilon_{nk} - \hbar\omega_{\mathbf{q}\lambda})$  and  $\delta(\varepsilon_{mk'} - \varepsilon_{nk} + \hbar\omega_{\mathbf{q}\lambda})$  expresses the absorption and emission of a phonon  $\omega_{\mathbf{q}\lambda}$ , respectively;  $n_{\mathbf{q}\lambda}$  denotes the phonon number under the Bose–Einstein distribution.

The harmonic interatomic force constants (IFCs) were obtained by the PHONOPY code [33] based on the density functional perturbation theory (DFPT) using a  $5 \times 5 \times 1$  ( $3 \times 3 \times 1$ ) supercell and a  $6 \times 6 \times 1$  ( $3 \times 3 \times 1$ )  $\mathbf{k}$ -mesh for both strained and unstrained  $\text{Se}_2\text{Te}$  ( $\text{SeTe}_2$ ) monolayers. We then obtained the phonon frequencies by diagonalized dynamic matrix. The finite displacement approach [33,34] was performed to calculate the IFCs with a  $4 \times 4 \times 1$  and a  $3 \times 3 \times 1$  supercell for  $\text{Se}_2\text{Te}$  and  $\text{SeTe}_2$  monolayers, respectively, considering the third nearest neighbors. Combining with the above calculated harmonic and anharmonic IFCs, the lattice thermal conductivity was evaluated using the ShengBTE code [35] by iterative solution of the phonon Boltzmann transport equation. After the lattice thermal conductivity convergence test, very dense  $\mathbf{q}$ -meshes of  $160 \times 160 \times 1$  and a scalebroad of 0.7 were employed in all calculations.

### 3. Results and Discussion

#### 3.1. Stability and Electronic Properties

The top and side views of the  $\alpha$ -phase  $\text{Se}_2\text{Te}$  and  $\text{SeTe}_2$  monolayers are shown in Figure 1. The same structure as 1T phase  $\text{MoS}_2$ ,  $\text{Se}_2\text{Te}$  and  $\text{SeTe}_2$  monolayers belong to the  $P\text{-}3m1$  space group and  $C_{3v}$  point group symmetry. After full relaxation, the lattice parameters are  $a = b = 3.98 \text{ \AA}$ , and  $a = b = 4.02 \text{ \AA}$  for  $\text{Se}_2\text{Te}$  and  $\text{SeTe}_2$  monolayers, respectively, agreeing well with the previous report [36]. To investigate the influence of tensile strain on materials properties, the in-plane biaxial tensile strain raised from biaxial tensile stress was considered, as depicted in Figure 1. The biaxial tensile strain is defined as,  $\varepsilon = (a - a_0)/a_0 \times 100\%$ , where  $a$  and  $a_0$  are the in-plane lattice parameter of the strained and unstrained monolayers, respectively.

Generally speaking, it is vital to check the stability of materials before calculating the properties. Thus, the phonon spectrums of  $\text{Se}_2\text{Te}$  and  $\text{SeTe}_2$  monolayers under unstrained and strained structures were investigated by PHONOPY code, as shown in Figure 2. It is found that there is no imaginary frequency in the Brillouin zone at the range of given tensile strain, such as 0–3% strain for  $\text{SeTe}_2$  and 0–1% strain for  $\text{Se}_2\text{Te}$ , suggesting that they are dynamic stability within a small tensile strain. Furthermore, tensile strain softens phonon mode, which may enhance the thermoelectric performance [13]. Overall, the longitudinal acoustic (LA) and transverse acoustic (TA) branches are linear near the  $\Gamma$  point, while the out-of-plane acoustic (ZA) branch is quadratic near the  $\Gamma$  point, and all of them shift to lower frequency upon the tensile strain.

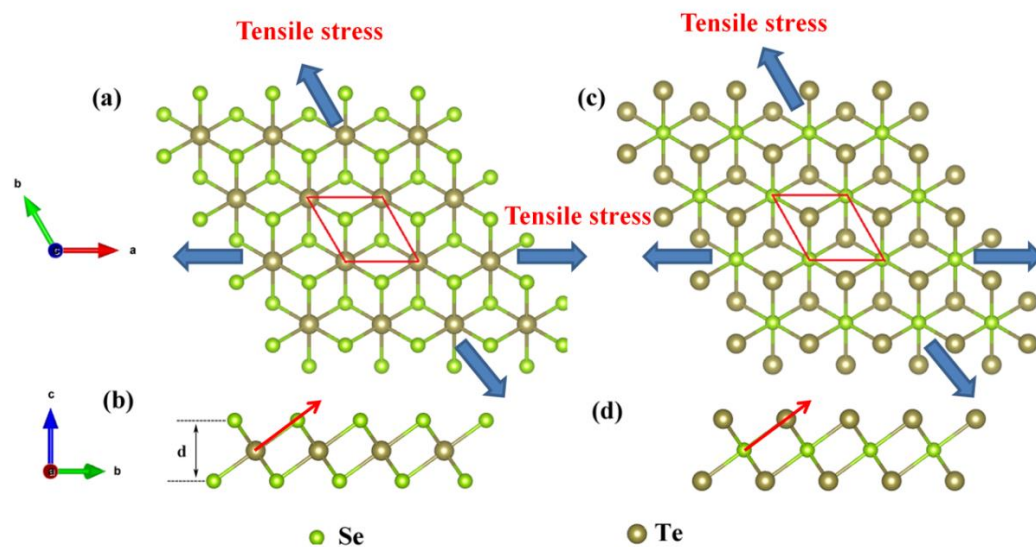


**Figure 1.** (Color online) Structure diagrams of  $\alpha$ -phase  $\text{Se}_2\text{Te}$  and  $\text{SeTe}_2$  monolayers. The (a) top and (b) side view of the  $\text{Se}_2\text{Te}$  monolayers, and (c) top and (d) side view of the  $\text{SeTe}_2$  monolayers. The blue arrow indicates the direction of tensile stress. The solid red diamond-shaped box represents the primitive cell. The red arrow demonstrates the direction of the ELF profile.

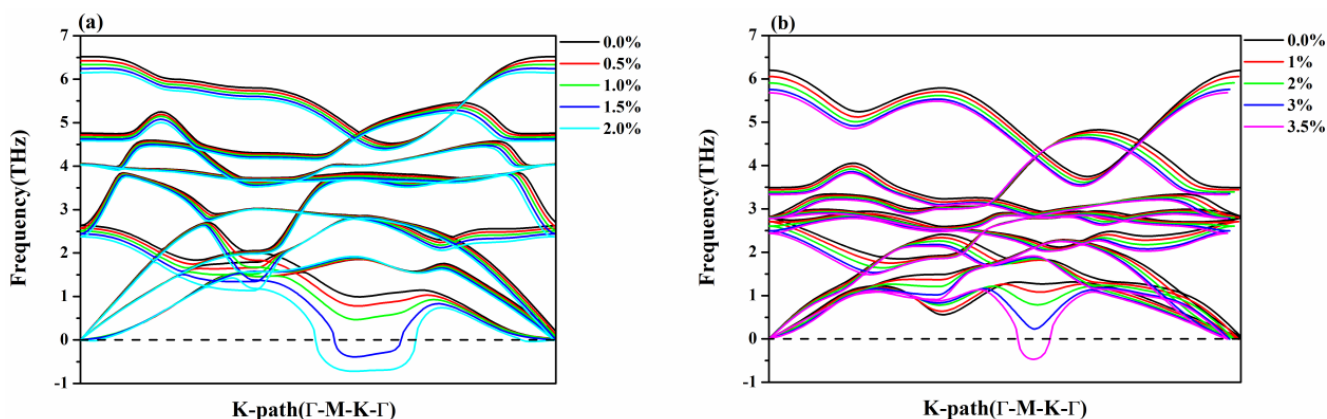


**Figure 2.** (Color online) Phonon dispersion curves under different tensile strains for (a)  $\text{Se}_2\text{Te}$  and (b)  $\text{SeTe}_2$  monolayers.

It is vital to correctly calculate the electronic band structure and total density of states (TDOS) related to the thermoelectric properties of a semiconductor [37,38]. It is well known that the SOC effect [39] plays a crucial role in the electronic band structure of materials containing heavy elements such as Te, thus the SOC effect is taken into account in the calculations. As depicted in Figure 3, the electric band structures and TDOS of unstrained and strained structures are calculated at the PBE + SOC level. For both  $\text{Se}_2\text{Te}$  and  $\text{SeTe}_2$  monolayers, it is found that the HOMO energy reduces with the tensile strains, while the LUMO energy enhances, leading to narrowing of the bandgap. Moreover, in Table 1, the influence of tensile strain on the bandgap of  $\text{Se}_2\text{Te}$  is significantly greater than that of  $\text{SeTe}_2$ . For example, the bandgap of  $\text{Se}_2\text{Te}$  is reduced by 11.11% under the effect of 1% tensile strain, while the bandgap of  $\text{SeTe}_2$  is reduced slightly by 3.79% under 3% tensile strain. This reduction of bandgap induced by strain results from the well-known rule that tensile strain increases the bond length between atoms, which leads to a decrease in the bandgap [14,40,41]. Furthermore, it is found that the TDOS of  $\text{Se}_2\text{Te}$  and  $\text{SeTe}_2$  monolayer under the Fermi level increases and shifts up as tensile strain increases, while the TDOS above the Fermi level remains almost the same in  $\text{Se}_2\text{Te}$  monolayer and decreases in the  $\text{SeTe}_2$  monolayer.

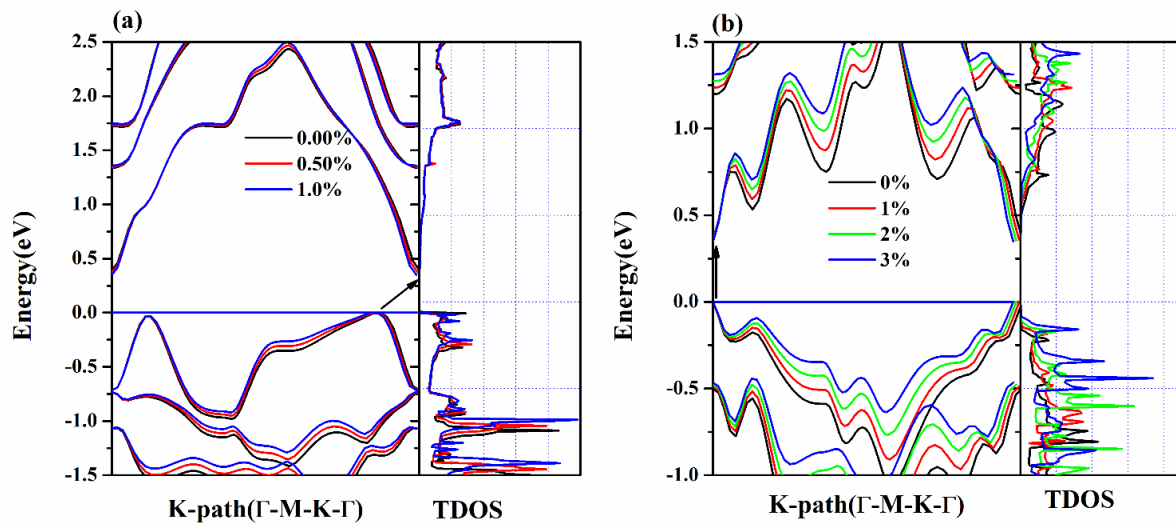


**Figure 3.** (Color online) Band structures and TDOS of (a)  $\text{Se}_2\text{Te}$  and (b)  $\text{SeTe}_2$  under various biaxial tensile strains.

**Table 1.** Deformation potential constants ( $E_1$ ) of  $\alpha$ -phase  $\text{SeTe}_2$  and  $\text{Se}_2\text{Te}$  based on PBE + SOC band structures under various tensile strains, together with the Young's modulus  $Y$ , elastic modulus  $C_{2D}$ , and bandgap  $E_g$ , respectively.

	Strain	$E_1^{\text{VBM}}$ (eV)	$E_1^{\text{CBM}}$ (eV)	$Y$ (GPa)	$C_{2D}$ (N/m)	$E_g$ (eV)
$\text{Se}_2\text{Te}$	0%	−5.086	−6.744	126.545	44.016	0.395
		−4.196 <sup>a</sup>	−6.676 <sup>a</sup>		43.64 <sup>a</sup>	0.38 <sup>a</sup>
	0.5%	−4.834	−6.552	123.247	42.547	0.373
	1%	−5.011	−6.512	120.317	41.178	0.351
$\text{SeTe}_2$	0%	−6.316	−6.446	103.340	37.538	0.363
		6.590 <sup>a</sup>	6.620 <sup>a</sup>		36.19 <sup>a</sup>	0.33 <sup>a</sup>
	1%	−6.098	−6.272	97.101	34.847	0.359
	2%	−5.782	−5.956	91.257	31.590	0.354
	3%	−5.568	−5.716	85.594	30.380	0.350

<sup>a</sup> Ref. [36].  $C_{2D}$  was calculated using the finite-difference method by Liu et al. [36].

Generally, the electron localization function (ELF) [42] can be used to determine the interaction type (chemical bonding type or physical binding type) between two atoms by measuring electron localization in the atomic and molecular systems [42,43]. The ELF is a relative measurement of the electron localization, and it takes values between 0 and 1 [44], where 1 corresponds to perfect localization, 0.5 means electron-gas-like pair probability, and 0 represents the absence of electrons. In other words, due to the lack of electrons sharing in the region between the two atoms, the value of ELF is very low, which represents the ionic binding; on the contrary, due to the abundant of electrons sharing in the region between the two atoms, the value of ELF is large, and it characterizes a covalent bond. To gain further insight into the effect of tensile strain on the character of the bond, we calculated ELF of  $\text{Se}_2\text{Te}$  and  $\text{SeTe}_2$  monolayers, as shown in Figure 4. Overall, it is found that all ELF are larger than 0.5 at tensile-strained circumstances, indicating that they are covalent bond compounds. Furthermore, the values of ELF decrease with the increasing strain, due to the increase in the length of chemical bonds between two atoms.

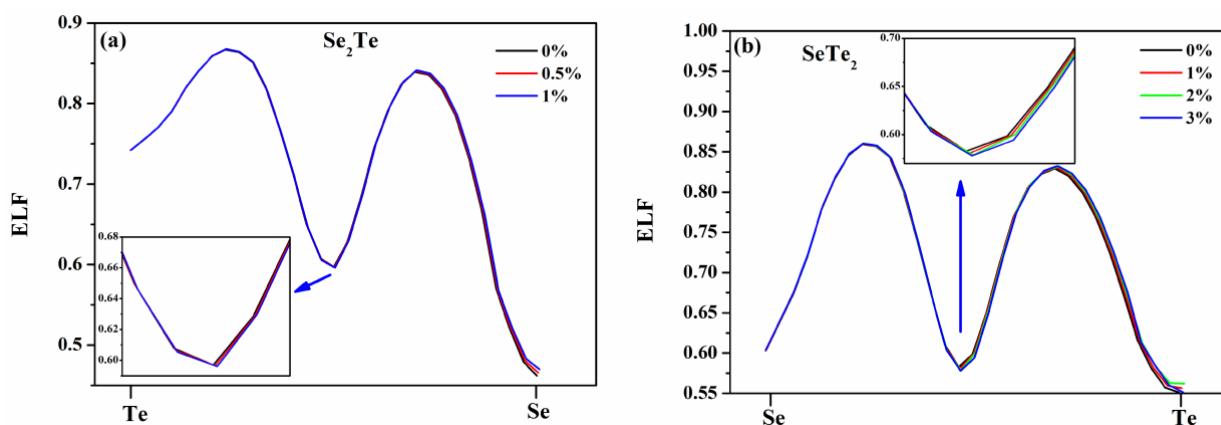


**Figure 4.** (Color online) The ELF profile from (a) Te to Se atom in the  $\text{Se}_2\text{Te}$  monolayers and (b) Se to Te atom in the  $\text{SeTe}_2$  monolayers as indicated by the red arrow in Figure 1b,d, respectively. The inset shows the ELF value of the middle region of the two atoms.

### 3.2. Electronic Transport Property

We then evaluated the electrical conductivity  $\sigma$ , Seebeck coefficient  $S$ , electronic thermal conductivity  $k_e$ , and thermoelectric power factor PF using the TransOpt package [22]. Deformation potential (DP)  $E_l$ , Young's modulus  $Y$ , and Fermi energy are the main input parameters for electronic transport performances, as shown in Table 1. The finite-difference method [45–49] was used to calculate the Young's modulus  $Y$ .  $E_l^{\text{VBM}}$  and  $E_l^{\text{CBM}}$  are the deformation potential of the VBM and CBM in the transport direction, respectively, which can be calculated by the formula:  $E_l = \frac{\partial E_{\text{edge}}}{\partial(\Delta l/l_0)}$ .  $E_{\text{edge}}$  is the energy of the VBM or CBM under slight uniaxial strain, ranging from  $-2\%$  to  $2\%$  in steps of  $0.5\%$ . The elastic modulus  $C_{2D}$  is evaluated by the formula:  $C_{2D} = \frac{1}{s_0} \frac{\partial^2 E}{\partial(\Delta l/l_0)^2}$ , where  $E$  is the total energy of materials under slight strain. The calculated  $C_{2D}$  agrees well with the results of Reference [36], indicating that the calculated results are reliable. As shown in Figure S1 (Supplemental Materials), the DP coefficient  $E_l$  is obtained by fitting the values of the band energies of the VBM and the CBM concerning the vacuum energy as a function of uniaxial strain. To reach convergence and obtain accurate calculation results, we used dense k-meshes of  $60 \times 60 \times 1$ .

From Figure 5, at given carrier concentration range, such as  $10^{19}$  to  $10^{20} \text{ cm}^{-3}$  and  $10^{19}$  to  $10^{21} \text{ cm}^{-3}$  for n- and p-type doping, respectively, all types of  $S$  approximately linearly decrease with increasing carrier concentration, while  $\sigma$  increases with carrier concentration. This can also be found in many other 2D materials that  $S$  and  $\sigma$  have a different relationship to carrier concentration since they have an opposite dependency with the DOS near the Fermi surface [7,37,50]. Thus, we can obtain the optimized PF shown in Figure 6 by the relationship of  $\text{PF} = S^2\sigma$ , which is a vital parameter for the figure of merit and is discussed in the following. Moreover, except for p-type doped  $S$  of  $\text{Se}_2\text{Te}$ , strain enhances the  $S$  as the increasing strain. Loosely speaking, the strain induces an enhancement of  $\sigma$  for  $\text{Se}_2\text{Te}$ , while it works oppositely for that of  $\text{SeTe}_2$ .

### 3.3. Lattice Thermal Conductivity

By comparison, the  $k_l$  of  $\text{SeTe}_2$  monolayers is much lower than that of  $\text{Se}_2\text{Te}$  monolayers, as shown in Figure 7, which is benefited from the large weight of the constituent elements [10] and weak bonding [51,52] (see Figure 4). Notably, it can be seen from Figure 7 that both the  $k_l$  of  $\text{Se}_2\text{Te}$  and  $\text{SeTe}_2$  decrease with the biaxial tensile strain. This may result from phonon softening [13].

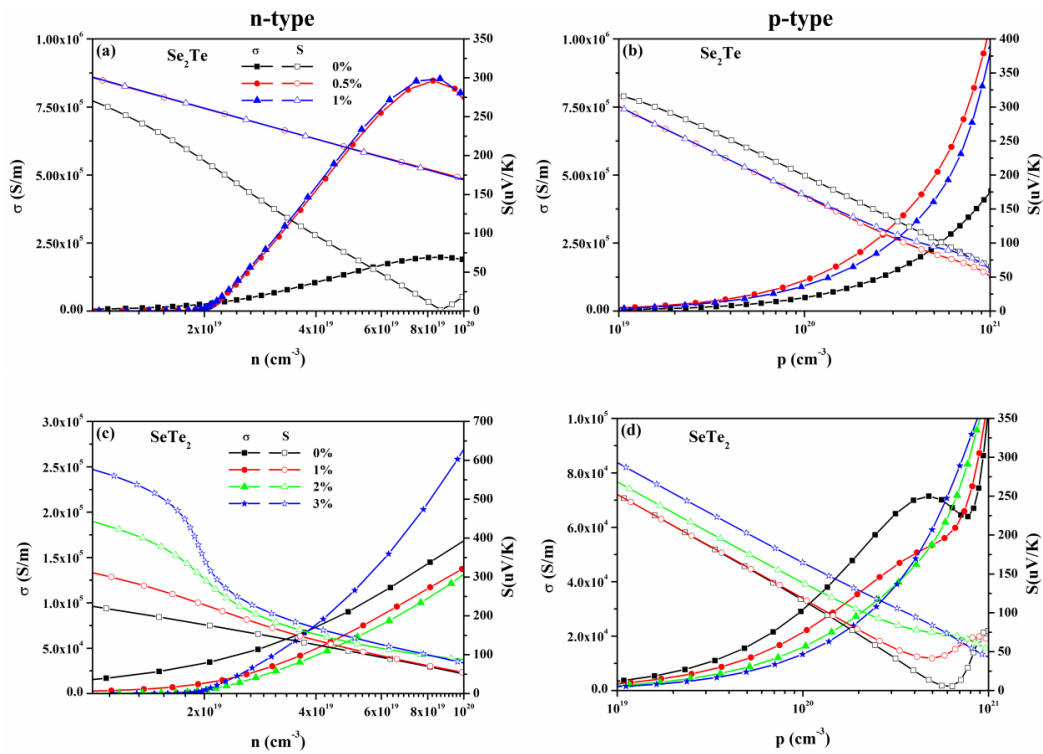


**Figure 5.** (Color online) The electronic conductivity  $\sigma$  and Seebeck coefficient  $S$  of (a,b)  $\text{Se}_2\text{Te}$  and (c,d)  $\text{SeTe}_2$  monolayers with different applied strain as a function of concentration for both n- and p-type doping at 300 K.

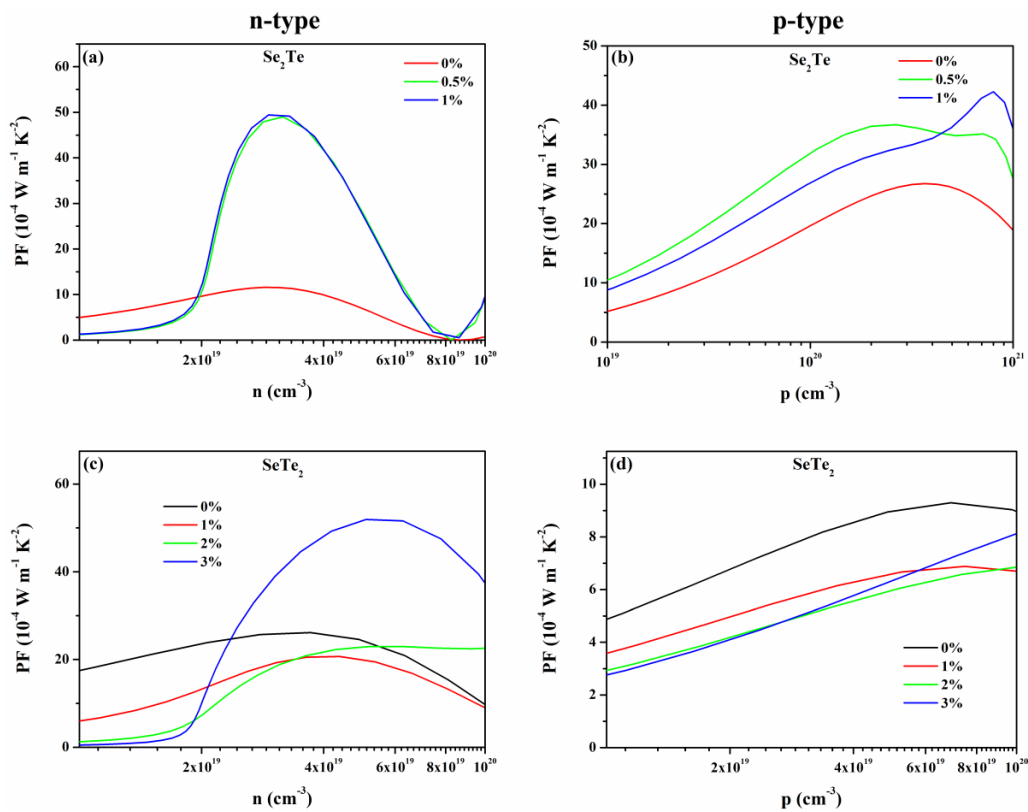


**Figure 6.** (Color online) The thermoelectric power factor PF of (a,b)  $\text{Se}_2\text{Te}$  and (c,d)  $\text{SeTe}_2$  monolayers under tensile strains at 300 K as a function of concentration, respectively.

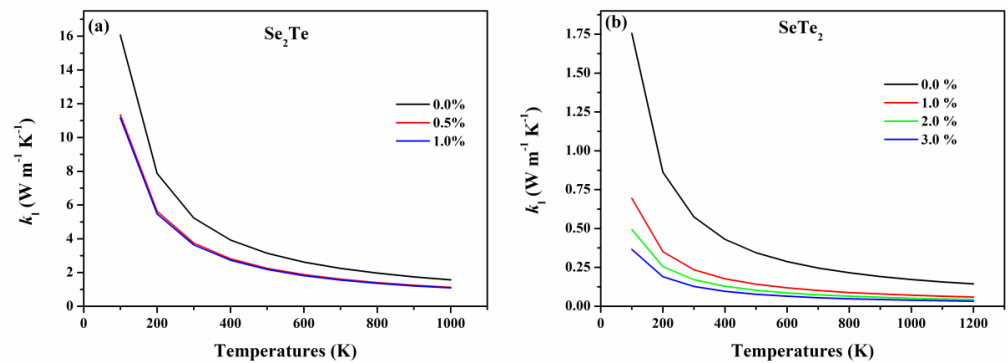


**Figure 7.** Strain-dependent lattice thermal conductivity  $k_l$  of (a)  $\text{Se}_2\text{Te}$  and (b)  $\text{SeTe}_2$  monolayers as a function of temperatures.

To further understand this reduction in  $k_l$  subjected to strain, we analyzed the effect of strain on phonon group velocities and phonon scattering rates as plotted in Figure 8. According to the calculated cumulative lattice thermal conductivity shown in Figure S2, we confirm that both  $\text{Se}_2\text{Te}$  and  $\text{SeTe}_2$  follow the conventional criteria that the lattice thermal conductivity is primarily carried by a low-frequency phonon, thus the phonon group velocity in the low-frequency range (0~2 THz) is plotted. Compared to  $\text{Se}_2\text{Te}$ , the scattering rate is superior in  $\text{SeTe}_2$  monolayers under unstrained and strained structures, while the opposite pattern appears in the low-frequency phonon group velocity, particularly at the long-wavelength limit. Thus, the  $\text{SeTe}_2$  monolayers possess lower  $k_l$  compared to that of the  $\text{Se}_2\text{Te}$  monolayers [53]. Loosely speaking, for both  $\text{Se}_2\text{Te}$  and  $\text{SeTe}_2$  monolayers, the tensile strain has opposite effects on the scattering rates and phonon group velocity, that is, the tensile strains generally increase the scattering rate while the group velocity is weakened by the tensile strain. As a result, the tensile strain distinctly reduces the value of  $k_l$ . Furthermore, at room temperature, the  $k_l$  of  $\text{Se}_2\text{Te}$  and  $\text{SeTe}_2$  monolayers reduced by 35.5% and 77.7% under 1% and 3% tensile strain, as summarized in Table 2, respectively. Hence, suitable tensile strain is favorable for thermoelectric performance by the reduction of the  $k_l$ , which is a very effective method to achieve enhanced  $ZT$ . Finally, by fitting the temperature-dependent  $k_l$ , it is found that  $k_l$  fulfills  $T^{-1}$  behavior in all circumstances, indicating a dominant Umklapp process of phonon scattering that causes thermal resistivity [11,50].

**Table 2.** Contributions of phonon modes (ZA, TA, LA, and all-optical) to total lattice thermal conductivity at 300 K, together with the lattice thermal conductivity  $k_l$ .

Compounds	Strain	ZA	TA	LA	Optical	$k_l$ ( $\text{W m}^{-1} \text{K}^{-1}$ )
$\text{Se}_2\text{Te}$	0%	17.73%	51.32%	23.65%	7.30%	5.236
	0.5%	19.28% [8]	43.12% [8]	28% [8]	9.29% [8]	4.88 [8]
	1%	18.28%	36.63%	35.50%	9.59%	3.744
	1%	21.90%	56.45%	14.14%	7.52%	3.636
$\text{SeTe}_2$	0%	11.49%	6.33%	65.42%	16.76%	0.574
	1%	14.98%	10.59%	48.23%	26.20%	0.235
	2%	12.96%	17.96%	37.62%	31.46%	0.171
	3%	14.74%	20.54%	32.85%	31.86%	0.128

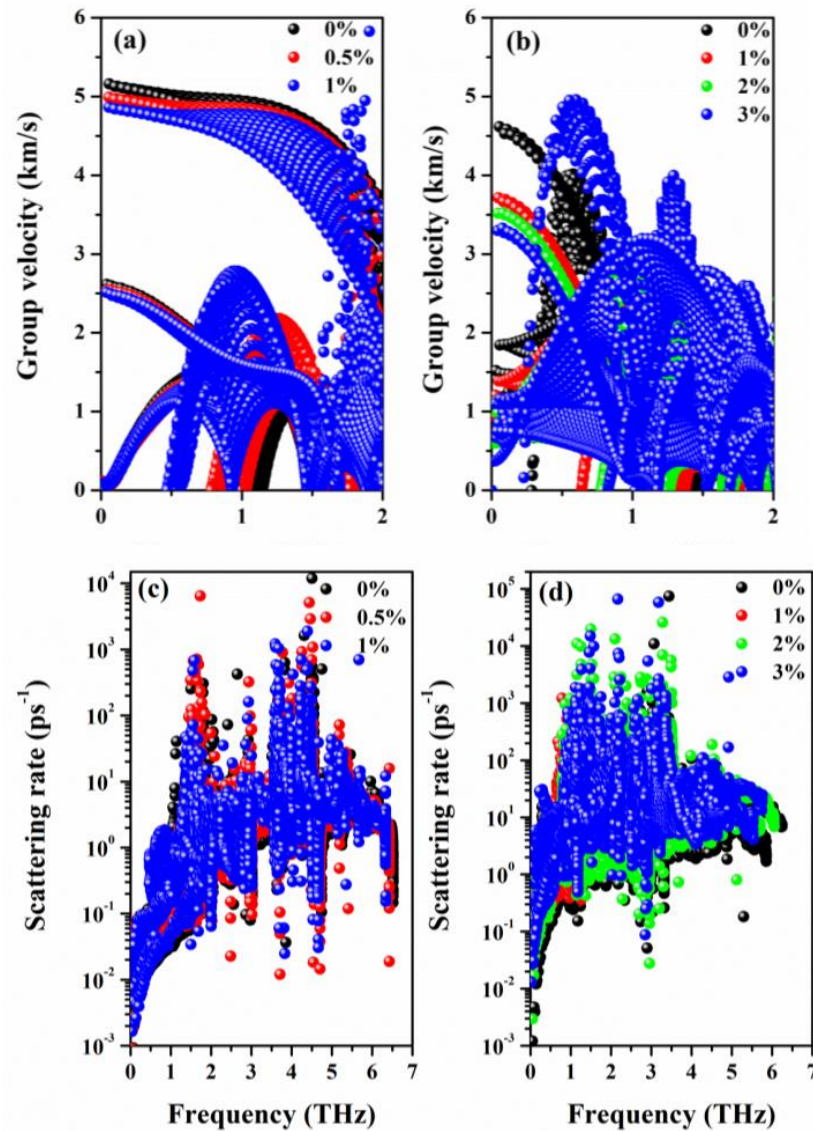


**Figure 8.** (Color online) The tensile-strained phonon group velocity of (a) Se<sub>2</sub>Te and (b) SeTe<sub>2</sub> monolayers. Phonon scattering rate of (c) Se<sub>2</sub>Te and (d) SeTe<sub>2</sub> under applied tensile strain.

### 3.4. Figure of Merit

To evaluate the size effect on the ballistic or diffusive phonon transport, we calculated the maximum phonon mean free path (MFP) distribution as plotted in Figure 9, which is important for thermal design with nanostructuring. In particular, by referring to the relationship between MFP and  $k_l$ , we can get better thermoelectric performance in the application of thermoelectric materials by effectively modulating  $k_l$ . To this end, at room temperature, the cumulative thermal conductivities  $k_l$  of the Se<sub>2</sub>Te and SeTe<sub>2</sub> monolayers as a function of the MFP under various biaxial strains are fitted to a single parametric function [35]:

$$k_l(\Lambda \leq \Lambda_{max}) = \frac{k_{l,max}}{1 + \frac{\Lambda_0}{\Lambda_{max}}} \quad (4)$$

where  $k_{l,max}$  is the maximum lattice thermal conductivity and  $\Lambda_{max}$  is the cutoff MFP. By fitting the cumulative thermal conductivity  $k_l$ , the phonon MFPs  $\Lambda_0$  of the Se<sub>2</sub>Te and SeTe<sub>2</sub> monolayers under different strains are obtained. The corresponding values are 39.70, 24.18, and 34.83 nm for Se<sub>2</sub>Te monolayers and 12.35, 1.29, 0.70, and 0.53 nm for SeTe<sub>2</sub> monolayers, respectively, which are much smaller than those of other 2D materials [54,55].

This indicates that  $k_1$  will significantly decrease when the size of the sample for  $\text{Se}_2\text{Te}$  and  $\text{SeTe}_2$  monolayers is below forty and twenty nanometers, respectively. Thus, our calculations provide an important reference for the subsequent material design. Notably, it found that the phonon MFPs decrease with increasing strains due to the integral decrease of MFP and higher contributions to  $k_1$  coming from the optical phonon branches [56], as summarized in Table 2.

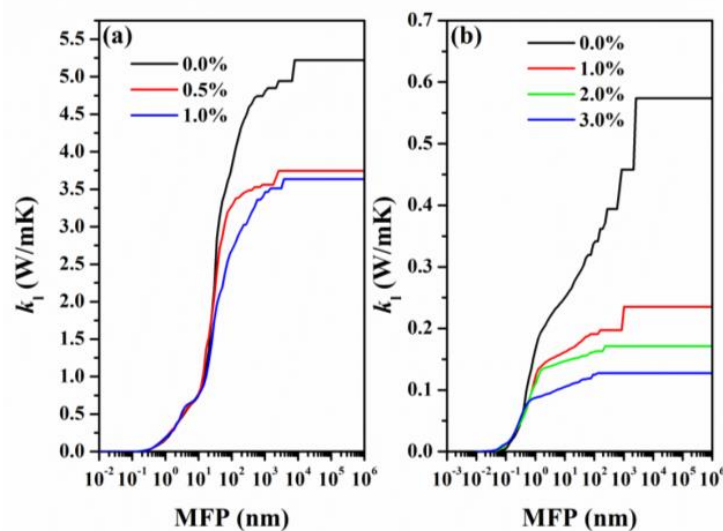


**Figure 9.** (Color online) The cumulative lattice thermal conductivity of (a)  $\text{Se}_2\text{Te}$  and (b)  $\text{SeTe}_2$  monolayers under tensile strains as a function of the phonon mean free path (MFP) at room temperature.

We then thoroughly studied the phonon mode contributions toward the  $k_1$  at 300 K from the acoustic phonon branches (ZA, TA, and LA) and optical branches (OP), as expressed in Table 2. By comparison, the phonon mode contributions to the  $k_1$  of unstrained  $\text{Se}_2\text{Te}$  monolayers are consistent with the report [8], and the value of  $k_1$  is also in agreement with that of the report. Moreover, it can be noticed that the  $k_1$  is mainly dominated by acoustic branches in all cases. One can easily see that the optical branches' contributions to the  $k_1$  increase with increasing biaxial strain, and at the same time the contributions of the acoustic phonon branches decrease.

To uncover the influence of biaxial strain on the thermoelectric conversion efficiency, we calculated the strain-dependent figure of merit  $ZT$  at  $T = 300$  K as a function of concentration, as shown in Figure 10. For unstrained structure, the p-type doping  $ZT$  of  $\text{Se}_2\text{Te}$  monolayers is superior to that of n-type doping, which is the opposite of that of  $\text{SeTe}_2$  monolayers. The reason for this discrepancy is interpreted in detail in our previous work [7]. For strained structures, overall, the value of n-type and p-type  $ZT$  was visibly enhanced for both  $\text{Se}_2\text{Te}$  and  $\text{SeTe}_2$  monolayers compared to that of the unstrained structures. Particularly, the maximum n-type doping  $ZT$  increases up to 1.38 (8.41) under 1% (3%) strain for the  $\text{Se}_2\text{Te}$  ( $\text{SeTe}_2$ ) monolayers, and this value is six (five) times higher than the corresponding  $ZT$  without strain. The corresponding maximum p-type doping  $ZT$  reaches up to 0.64 (1.67), which is 1.6 (2.5) times higher than that of unstrained structures. Such a high value of  $ZT$  of strained structures is larger than those of most reported 2D materials, such as  $\alpha$ -Te [57],  $\text{SiTe}_2$  [58],  $\text{SnTe}_2$  [58], and  $\text{XSe}$  ( $X = \text{Ge}, \text{Sn}, \text{and Pb}$ ) [50], and even larger than typically single and polycrystalline crystal  $\text{SnSe}$  [59,60], indicating tensile strain is an effective category to enhance the thermoelectric effect.

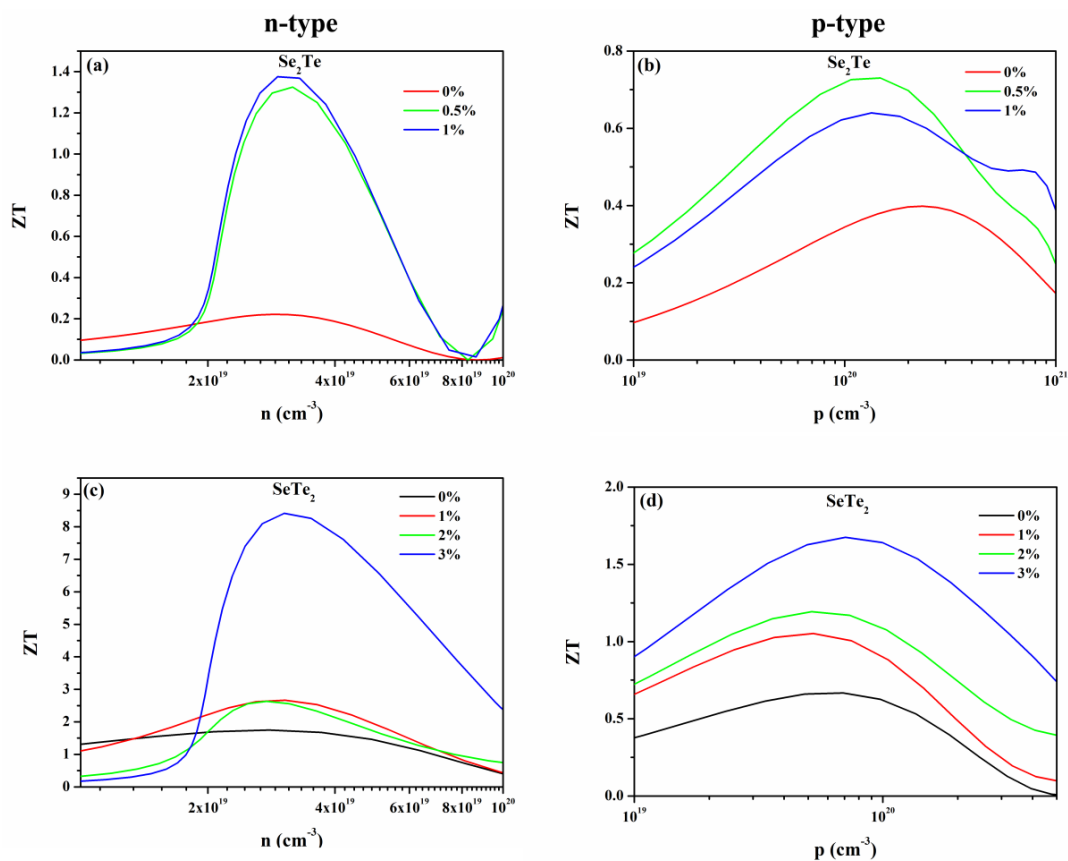


**Figure 10.** (Color online) The strain-dependent figure of merit  $ZT$  of (a,b)  $\text{Se}_2\text{Te}$  and (c,d)  $\text{SeTe}_2$  monolayers at room temperature as a function of concentration, respectively.

Moreover, it is also found that, except for n-type doped  $\text{Se}_2\text{Te}$  and p-type doped  $\text{SeTe}_2$ , the value of  $ZT$  does not increase monotonously as strain increases. Unlike the  $\text{SeTe}_2$  monolayers, the type of relatively large  $ZT$  value of the  $\text{Se}_2\text{Te}$  monolayers has changed with applied strain, i.e., for the strained structure, the n-type  $ZT$  is greater than the p-type  $ZT$ , which is exactly the opposite of the unstrained structure. To reveal those phenomena and the reason how strain greatly enhanced thermoelectric performance, we calculated the PF and  $k_e$ , as plotted in Figure 6 and Figure S3, respectively, due to PF and  $k_e$  being vital parameters according to the formula  $ZT = PF \cdot T / (k_e + k_l)$ . Combining with the previously calculated  $k_l$ , except for the p-type doped  $\text{SeTe}_2$  monolayers, the enhancement of thermoelectric performance induced by the strain is attributed to the simultaneous increase of the PF and decrease of the  $k_l$ , which has also been found in other reports [13,61]. Although p-type PF decrease compared to the unstrained  $\text{SeTe}_2$  monolayers, the thermal conductivity decreases and it dominates, resulting in an enhancement of  $ZT$ . An interesting observation in our calculations shows that, for p-type  $\text{Se}_2\text{Te}$  and n-type  $\text{SeTe}_2$ , the value of  $ZT$  does not increase monotonously with strain, which is a result of the complicated change of PF,  $k_e$ , and  $k_l$ .

#### 4. Conclusions

We evaluated the influence of biaxial-tensile strain on the stability, electronic properties, lattice thermal conductivity, and thermoelectric performance of  $\alpha$ -phase  $\text{Se}_2\text{Te}$  and  $\text{SeTe}_2$  monolayers by first-principle calculations combined with the semiclassical Boltzmann theory. It is found that small tensile strain softens the phonon model and reduces the phonon frequency, at the same time, the tensile strain strengthens the scattering rate and weakens the group velocity, resulting in a reduction of the lattice thermal conductivity  $k_l$ . The tensile strain increases the bond length, which leads to a decrease in the bandgap. Furthermore, simultaneously combined with the weakened  $k_l$ , the tensile strain can also

effectively modulate the electronic transport coefficients, such as electronic conductivity, Seebeck coefficient, and electronic thermal conductivity, to greatly enhance the value of  $ZT$ . Our calculations indicated tensile strain can effectively enhance the thermoelectric performance of  $\text{Se}_2\text{Te}$  and  $\text{SeTe}_2$  monolayers.

**Supplementary Materials:** The following are available online at <https://www.mdpi.com/article/10.3390/nano12010040/s1>, Figure S1: The strain-dependent deformation potential constants  $E_1$  of  $\alpha$ -phase (a-f)  $\text{Se}_2\text{Te}$  and (g-n)  $\text{SeTe}_2$  monolayer based on PBE + SOC band structures, respectively. The red straight line is the linear fitting curve; Figure S2: The strain-dependent cumulative  $k_1$  of (a)  $\text{Se}_2\text{Te}$  and (b)  $\text{SeTe}_2$  monolayer at 300 K as a function of frequency; Figure S3: The strain-dependent electronic thermal conductivity  $k_e$  of (a, b)  $\text{Se}_2\text{Te}$  and (c, d)  $\text{SeTe}_2$  monolayer at 300 K as a function of concentration for n-type and p-type doping, respectively.

**Author Contributions:** Conceptualization, X.-R.C. and C.-E.H.; methodology, S.-B.C.; software, H.-Y.G.; validation, X.-R.C.; formal analysis, S.-B.C. and W.-J.Y.; investigation, S.-B.C.; resources, G.L.; data curation, X.-R.C. and S.-B.C.; writing—original draft preparation, S.-B.C.; writing—review and editing, S.-B.C., X.-R.C. and G.L.; visualization, C.-E.H.; supervision, S.-B.C.; project administration, S.-B.C.; funding acquisition, S.-B.C., W.-J.Y. and X.-R.C. All authors have read and agreed to the published version of the manuscript.

**Funding:** Please add: This research was funded by the National Natural Science Foundation of China, grant number 12074274, the NSAF, grant number U1830101, the Guizhou Education Department Youth Science and Technology Talents Growth Project, grant number [2018]333, and the Anshun University Key Laboratory of Materials Simulation and Computing, grant number Asxyxkpt201803.

**Institutional Review Board Statement:** Not applicable.

**Informed Consent Statement:** Not applicable.

**Data Availability Statement:** Not applicable.

**Conflicts of Interest:** Declare conflicts of interest or state.

## References

1. Zhang, X.; Zhao, L.D. Thermoelectric materials: Energy conversion between heat and electricity. *J. Mater. Chem.* **2015**, *1*, 92–105. [[CrossRef](#)]
2. Bell, L.E. Cooling, heating, generating power, and recovering waste heat with thermoelectric systems. *Science* **2008**, *321*, 1457–1461. [[CrossRef](#)]
3. Ouyang, Y.; Zhang, Z.; Li, D.; Chen, J.; Zhang, G. Emerging Theory, Materials, and Screening Methods: New Opportunities for Promoting Thermoelectric Performance. *Ann. Der Phys.* **2019**, *531*, 1800437. [[CrossRef](#)]
4. Zhu, Z.L.; Cai, X.L.; Yi, S.H.; Chen, J.L.; Dai, Y.W.; Niu, C.Y.; Guo, Z.X.; Xie, M.H.; Liu, F.; Cho, J.H.; et al. Multivalency-driven formation of Te-based monolayer materials: A combined first-principles and experimental study. *Phys. Rev. Lett.* **2017**, *119*, 5. [[CrossRef](#)] [[PubMed](#)]
5. Chen, J.; Dai, Y.; Ma, Y.; Dai, X.; Ho, W.; Xie, M. Ultrathin beta-tellurium layers grown on highly oriented pyrolytic graphite by molecular-beam epitaxy. *Nanoscale* **2017**, *9*, 15945–15948. [[CrossRef](#)]
6. Lin, Z.Y.; Wang, C.; Chai, Y. Emerging Group-VI Elemental 2D Materials: Preparations, Properties, and Device Applications. *Small* **2020**, *16*, 16. [[CrossRef](#)]
7. Chen, S.; Tao, W.; Zhou, Y.; Zeng, Z.; Chen, X.; Geng, H. Novel thermoelectric performance of 2D 1T- $\text{Se}_2\text{Te}$  and  $\text{SeTe}_2$  with ultralow lattice thermal conductivity but high carrier mobility. *Nanotechnology* **2021**, *32*, 455401. [[CrossRef](#)] [[PubMed](#)]
8. Zhong, X.; Huang, Y.; Yang, X. Superior thermoelectric performance of  $\alpha$ - $\text{Se}_2\text{Te}$  monolayer. *Mater. Res. Express* **2021**, *8*, 045507. [[CrossRef](#)]
9. Liu, Y.; Wu, W.; Goddard, W.A. Tellurium: Fast Electrical and Atomic Transport along the Weak Interaction Direction. *J. Am. Chem. Soc.* **2018**, *140*, 550–553. [[CrossRef](#)]
10. Ramírez-Montes, L.; López-Pérez, W.; González-Hernández, R.; Pinilla, C. Large thermoelectric figure of merit in hexagonal phase of 2D selenium and tellurium. *Int. J. Quantum Chem.* **2020**, *120*, 26267. [[CrossRef](#)]
11. Gao, Z.; Tao, F.; Ren, J. Unusually low thermal conductivity of atomically thin 2D tellurium. *Nanoscale* **2018**, *10*, 12997–13003. [[CrossRef](#)]
12. Sharma, M. Stability, Tunneling Characteristics and Thermoelectric Properties of  $\text{TeSe}_2$  allotropes. *arXiv* **2020**, arXiv:2012.03871.
13. Lv, H.Y.; Lu, W.J.; Shao, D.F.; Lu, H.Y.; Sun, Y.P. Strain-induced enhancement in the thermoelectric performance of a  $\text{ZrS}_2$  monolayer. *J. Mater. Chem. C* **2016**, *4*, 4538–4545. [[CrossRef](#)]
14. Guo, S.-D. Biaxial strain tuned thermoelectric properties in monolayer  $\text{PtSe}_2$ . *J. Mater. Chem. C* **2016**, *4*, 9366–9374. [[CrossRef](#)]

15. D'Souza, R.; Mukherjee, S.; Ahmad, S. Strain induced large enhancement of thermoelectric figure-of-merit (ZT similar to 2) in transition metal dichalcogenide monolayers ZrX<sub>2</sub> (X = S, Se, Te). *J. Appl. Phys.* **2019**, *126*, 214302. [[CrossRef](#)]
16. Wang, N.; Li, M.; Xiao, H.; Gong, H.; Liu, Z.; Zu, X.; Qiao, L. Optimizing the thermoelectric transport properties of Bi<sub>2</sub>O<sub>2</sub>Se monolayer via biaxial strain. *Phys. Chem. Chem. Phys.* **2019**, *21*, 15097–15105. [[CrossRef](#)]
17. Kresse, G.; Furthmüller, J. Efficient iterative schemes for ab initio total-energy calculations using a plane-wave basis set. *Phys. Rev. B* **1996**, *54*, 11169–11186. [[CrossRef](#)] [[PubMed](#)]
18. Kresse, G.; Furthmüller, J. Efficiency of ab-initio total energy calculations for metals and semiconductors using a plane-wave basis set. *Comp. Mater. Sci.* **1996**, *6*, 15–50. [[CrossRef](#)]
19. Perdew, J.P.; Burke, K.; Ernzerhof, M. Generalized Gradient Approximation Made Simple. *Phys. Rev. Lett.* **1996**, *77*, 3865–3868. [[CrossRef](#)] [[PubMed](#)]
20. Eglitis, R.I.; Purans, J.; Jia, R. Comparative Hybrid Hartree-Fock-DFT Calculations of WO<sub>2</sub>-Terminated Cubic WO<sub>3</sub> as Well as SrTiO<sub>3</sub>, BaTiO<sub>3</sub>, PbTiO<sub>3</sub> and CaTiO<sub>3</sub> (001) Surfaces. *Crystals* **2021**, *11*, 455. [[CrossRef](#)]
21. Eglitis, R.I.; Purans, J.; Popov, A.I.; Jia, R. Tendencies in ABO<sub>3</sub> Perovskite and SrF<sub>2</sub>, BaF<sub>2</sub> and CaF<sub>2</sub> Bulk and Surface F-Center Ab Initio Computations at High Symmetry Cubic Structure. *Symmetry* **2021**, *13*, 1920. [[CrossRef](#)]
22. Li, X.; Zhang, Z.; Xi, J.; Singh, D.J.; Sheng, Y.; Yang, J.; Zhang, W. TransOpt. A code to solve electrical transport properties of semiconductors in constant electron-phonon coupling approximation. *Comp. Mater. Sci.* **2021**, *186*, 110074. [[CrossRef](#)]
23. Ding, J.; Liu, C.; Xi, L.; Xi, J.; Yang, J. Thermoelectric transport properties in chalcogenides ZnX (X = S, Se): From the role of electron-phonon couplings. *J. Materiomics* **2021**, *7*, 310–319. [[CrossRef](#)]
24. Sheng, Y.; Wu, Y.; Yang, J.; Lu, W.; Villars, P.; Zhang, W. Active learning for the power factor prediction in diamond-like thermoelectric materials. *Npj Comput. Mater.* **2020**, *6*, 171. [[CrossRef](#)]
25. Xi, L.; Pan, S.; Li, X.; Xu, Y.; Ni, J.; Sun, X.; Yang, J.; Luo, J.; Xi, J.; Zhu, W. Discovery of High Performance Thermoelectric Chalcogenides through Reliable High Throughput Material Screening. *J. Am. Chem. Soc.* **2018**, *140*, 10785–10793. [[CrossRef](#)]
26. Li, R.; Li, X.; Xi, L.; Yang, J.; Singh, D.J.; Zhang, W. High-Throughput Screening for Advanced Thermoelectric Materials: Diamond-Like ABX<sub>2</sub> Compounds. *ACS Appl. Mater. Interfaces* **2019**, *11*, 24859–24866. [[CrossRef](#)]
27. Madsen, G.K.H.; Singh, D.J. BoltzTraP. A code for calculating band-structure dependent quantities. *Comput. Phys. Commun.* **2006**, *175*, 67–71. [[CrossRef](#)]
28. Madsen, G.K.H.; Carrete, J.; Verstraete, M.J. BoltzTraP2, a program for interpolating band structures and calculating semi-classical transport coefficients. *Comput. Phys. Commun.* **2018**, *231*, 140–145. [[CrossRef](#)]
29. Yang, J.; Xi, L.; Qiu, W.; Wu, L.; Shi, X.; Chen, L.; Yang, J.; Zhang, W.; Uher, C.; Singh, D.J. On the tuning of electrical and thermal transport in thermoelectrics: An integrated theory-experiment perspective. *Npj Comput. Mater.* **2016**, *2*, 15015. [[CrossRef](#)]
30. Neophytou, N.; Kosina, H. Effects of confinement and orientation on the thermoelectric power factor of silicon nanowires. *Phys. Rev. B* **2011**, *83*, 1971–1980. [[CrossRef](#)]
31. Xi, J.Y.; Wang, D.; Yi, Y.P.; Shuai, Z.G. Electron-phonon couplings and carrier mobility in graphynes sheet calculated using the Wannier-interpolation approach. *J. Chem. Phys.* **2014**, *141*, 10. [[CrossRef](#)]
32. Xi, J.; Long, M.; Tang, L.; Wang, D.; Shuai, Z. First-principles prediction of charge mobility in carbon and organic nanomaterials. *Nanoscale* **2012**, *4*, 4348–4369. [[CrossRef](#)]
33. Togo, A.; Oba, F.; Tanaka, I. First-principles calculations of the ferroelastic transition between rutile-type and CaCl<sub>2</sub>-type SiO<sub>2</sub> at high pressures. *Phys. Rev. B* **2008**, *78*, 134106. [[CrossRef](#)]
34. Baroni, S.; De Gironcoli, S.; Corso, D.A.; Gianozzi, P. Phonons and related crystal properties from density-functional perturbation theory. *Rev. Mod. Phys.* **2001**, *73*, 515–562. [[CrossRef](#)]
35. Li, W.; Carrete, J.; Katcho, N.A.; Mingo, N. Sheng BTE: A solver of the Boltzmann transport equation for phonons. *Comput. Phys. Commun.* **2014**, *185*, 1747–1758. [[CrossRef](#)]
36. Liu, G.; Wang, H.; Li, G.-L. Structures, mobilities, electronic and optical properties of two-dimensional  $\alpha$ -phase group-VI binary compounds:  $\alpha$ -Se<sub>2</sub>Te and  $\alpha$ -SeTe<sub>2</sub>. *Phys. Lett. A* **2020**, *384*, 126431. [[CrossRef](#)]
37. Kumar, S.; Schwingenschloegl, U. Thermoelectric response of bulk and monolayer MoSe<sub>2</sub> and WSe<sub>2</sub>. *Chem. Mater.* **2015**, *27*, 1278–1284. [[CrossRef](#)]
38. Zhu, X.L.; Liu, P.F.; Xie, G.; Zhou, W.X.; Wang, B.T.; Zhang, G. Thermoelectric Properties of Hexagonal M<sub>2</sub>C<sub>3</sub> (M = As, Sb, and Bi) Monolayers from First-Principles Calculations. *Nanomaterials* **2019**, *9*, 597. [[CrossRef](#)] [[PubMed](#)]
39. Hummer, K.; Grüneis, A.; Kresse, G. Structural and electronic properties of lead chalcogenides from first principles. *Phys. Rev. B* **2007**, *75*, 195211. [[CrossRef](#)]
40. Huang, W.; Yang, H.; Cheng, B.; Xue, C. Theoretical study of the bandgap regulation of a two-dimensional GeSn alloy under biaxial strain and uniaxial strain along the armchair direction. *Phys. Chem. Chem. Phys.* **2018**, *20*, 23344–23351. [[CrossRef](#)]
41. Guan, X.; Zhu, G.; Wei, X.; Cao, J. Tuning the electronic properties of monolayer MoS<sub>2</sub>, MoSe<sub>2</sub> and MoSSe by applying z-axial strain. *Chem. Phys. Lett.* **2019**, *730*, 191–197. [[CrossRef](#)]
42. Becke, A.D.; Edgecombe, K.E. A simple measure of electron localization in atomic and molecular systems. *J. Chem. Phys.* **1990**, *92*, 5397–5403. [[CrossRef](#)]
43. Koumpouras, K.; Larsson, J.A. Distinguishing between chemical bonding and physical binding using electron localization function (ELF). *J. Phys. Condens. Matter* **2020**, *32*, 315502. [[CrossRef](#)] [[PubMed](#)]

44. Steinmann, S.N.; Mo, Y.; Corminboeuf, C. How do electron localization functions describe  $\pi$ -electron delocalization? *Phys. Chem. Chem. Phys.* **2011**, *13*, 20584–20592. [[CrossRef](#)]
45. Page, Y.L.; Saxe, P. Symmetry-general least-squares extraction of elastic data for strained materials from ab initio calculations of stress. *Phys. Rev. B* **2002**, *65*, 104104. [[CrossRef](#)]
46. Blonsky, M.N.; Zhuang, H.L.; Singh, A.K.; Hennig, R.G. Ab initio prediction of piezoelectricity in two-dimensional materials. *ACS Nano* **2015**, *9*, 9885–9891. [[CrossRef](#)]
47. Alyörük, M.M.; Aierken, Y.; Çakır, D.; Peeters, F.M.; Sevik, C. Promising piezoelectric performance of single layer transition-metal dichalcogenides and dioxides. *J. Phys. Chem. C* **2015**, *119*, 23231–23237. [[CrossRef](#)]
48. Çakır, D.; Peeters, F.M.; Sevik, C. Mechanical and thermal properties of h-MX<sub>2</sub> (M = Cr, Mo, W; X = O, S, Se, Te) monolayers: A comparative study. *Appl. Phys. Lett.* **2014**, *104*, 203110. [[CrossRef](#)]
49. Yin, H.; Gao, J.; Zheng, G.; Wang, Y.; Ma, Y. Giant Piezoelectric Effects in Monolayer Group-V Binary Compounds with Honeycomb Phases: A First-Principles Prediction. *J. Mater. Chem. C* **2017**, *121*, 25576–25584. [[CrossRef](#)]
50. Zhu, X.-L.; Hou, C.-H.; Zhang, P.; Liu, P.-F.; Xie, G.; Wang, B.-T. High thermoelectric performance of new two-dimensional IV–VI compounds: A first-principles study. *J. Phys. Chem. C* **2020**, *124*, 1812–1819. [[CrossRef](#)]
51. Spitzer, D.P. Lattice thermal conductivity of semiconductors: A chemical bond approach. *J. Phys. Chem. Solids* **1970**, *31*, 19–40. [[CrossRef](#)]
52. Feng, Z.; Fu, Y.; Zhang, Y.; Singh, D.J. Characterization of rattling in relation to thermal conductivity: Ordered half-Heusler semiconductors. *Phys. Rev. B* **2020**, *101*, 064301. [[CrossRef](#)]
53. Muthaiah, R.; Tarannum, F.; Garg, J. Strain tuned low thermal conductivity in Indium Antimonide (InSb) through increase in anharmonic phonon scattering—A first-principles study. *Solid State Commun.* **2021**, *334–335*, 114378. [[CrossRef](#)]
54. Peng, B.; Zhang, H.; Shao, H.; Xu, Y.; Zhang, X.; Zhu, H. Low lattice thermal conductivity of stanene. *Sci. Rep.* **2016**, *6*, 20225. [[CrossRef](#)]
55. Shafique, A.; Samad, A.; Shin, Y.-H. Ultra low lattice thermal conductivity and high carrier mobility of monolayer SnS<sub>2</sub> and SnSe<sub>2</sub>: A first principles study. *Phys. Chem. Chem. Phys.* **2017**, *19*, 20677–20683. [[CrossRef](#)] [[PubMed](#)]
56. Qin, G.; Qin, Z.; Fang, W.Z.; Zhang, L.C.; Su, G. Diverse anisotropy of phonon transport in two-dimensional IV–VI compounds: A comparative study. *Nanoscale* **2016**, *8*, 11306. [[CrossRef](#)]
57. Ma, J.; Meng, F.; He, J.; Jia, Y.; Li, W. Strain-Induced Ultrahigh Electron Mobility and Thermoelectric Figure of Merit in Monolayer  $\alpha$ -Te. *ACS Appl. Mater. Interfaces* **2020**, *12*, 43901–43910. [[CrossRef](#)]
58. Wang, Y.; Gao, Z.B.; Zhou, J. Ultralow lattice thermal conductivity and electronic properties of monolayer 1T phase semimetal SiTe<sub>2</sub> and SnTe<sub>2</sub>. *Physica E* **2019**, *108*, 53–59. [[CrossRef](#)]
59. Zhao, L.D.; Lo, S.H.; Zhang, Y.; Sun, H.; Tan, G.; Uher, C.; Wolverton, C.; Dravid, V.P.; Kanatzidis, M.G. Ultralow thermal conductivity and high thermoelectric figure of merit in SnSe crystals. *Nature* **2014**, *508*, 373–377. [[CrossRef](#)]
60. Lou, X.; Li, S.; Chen, X.; Zhang, Q.; Deng, H.; Zhang, J.; Li, D.; Zhang, X.; Zhang, Y.; Zeng, H.; et al. Lattice Strain Leads to High Thermoelectric Performance in Polycrystalline SnSe. *ACS Nano* **2021**, *15*, 8204–8215. [[CrossRef](#)]
61. Cicek, M.M.; Demirtas, M.; Durgun, E. Tuning thermoelectric efficiency of monolayer indium nitride by mechanical strain. *J. Appl. Phys.* **2021**, *129*, 234302. [[CrossRef](#)]